Check for updates

ADVANCED FUNCTIONAL MATERIALS
www.afm-journal.de

Thermal Expansion Behavior of PM6 Studied Using In Situ Wide-Angle X-Ray Scattering

*Meike Kuhn, Xu Huang, Matthew Gebert, Lars Thomsen, Christopher R. McNeill, and Eva M. Herzig**

In organic photovoltaics, even small morphological changes on the sub-nanometer scale can significantly impact the device's performance. Such structural changes intrinsically occur due to the thermal response of a material, making a fundamental understanding of these processes essential. In this study, the thermal expansion of the high-performance donor material PDBD-T-2F (PM6) is characterized using in situ transmission and grazing incidence wide-angle X-ray scattering (WAXS and GIWAXS) over the temperature range of 30–300 °C. By systematically increasing the complexity of the sample, multiple influencing factors are deciphered. Significantly, distinct structural differences and temperature expansion behavior is observed for the face-on and edge-on crystallite fraction. In particular, the initial lamellar stacking *d*-spacings differ for the two fractions and moreover, the face-on fraction exhibits significantly lower thermal expansion in lamellar direction compared to the edge-on fraction. In situ GIWAXS measurements performed during solution coating show that these differences are formed during film formation. Additionally, an impact of the thermal expansion mismatch between the substrate and the sample is observed, limiting the in-plane π–π stacking expansion. The results emphasize the interplay between molecular packing, substrate interaction, and thermal response.

1. Introduction

In recent years, interest in semiconducting polymer materials has significantly increased due to their potential application in organic solar cells (OSCs), organic field effect transistors, organic electrochemical transistors, and organic thermoelectrics.[1–4] Advantages, such as ease of processing, flexibility, and low weight that can be realized for large-area devices, make semiconducting polymers a promising candidate for future developments. Since the discovery of non-fullerene acceptors (NFAs), record efficiencies of over 19% have been reached for polymer-NFA blends in organic solar cells.[5–7] Among these, the combination of the donor polymer PM6 (also known as PDBD-T-2F) with the small-molecule acceptor Y6 has attracted significant attention. This is due to their complementary absorption profile, which covers a broad range of the solar spectrum[8,9] as well as their favorable charge transport properties.[10–12] Semiconducting polymers are typically classified into six structural categories: amorphous, oriented amorphous, highly disordered, 2D semi-paracrystalline, 3D semi-paracrystalline, and crystalline, based on their melting behavior and degree of disorder.[13] Due to the absence of a detectable melting point in conventional calorimetry, PM6 has been classified as a highly disordered polymer.[13] However, recent studies using fast-scanning calorimetry have reported a melting point above 400 °C, suggesting that PM6 is a semi-paracrystalline material, with paracrystallites coexisting alongside disordered regions.[14] Furthermore, changes in the melting point can be correlated with the microstructure of the thin film.[14] These findings indicate that fundamental properties such as the melting point can be influenced by the microstructure of the sample. However, it remains unclear which additional factors affect the thermal response of PM6, especially within a thin film. In this study, we examine the film formation and thermal behavior of PM6 thin films using in situ transmission and grazing incidence wide-angle X-ray scattering (WAXS and GIWAXS). Scattering patterns were recorded as a function of time during film formation and as a function of temperature during heating and cooling between 30 and 300 °C. We investigate the potential influence of the following factors on the

M. Kuhn, E. M. Herzig
Dynamics and Structure Formation – Herzig Group
Institute of Physics
University of Bayreuth
95447 Bayreuth, Germany
E-mail: eva.herzig@uni-bayreuth.de

M. Kuhn, X. Huang, M. Gebert, C. R. McNeill, E. M. Herzig
Department of Materials Science and Engineering
Monash University
Clayton, Victoria 3800, Australia

L. Thomsen
Australian Synchrotron
ANSTO
Clayton, Victoria 3168, Australia

The ORCID identification number(s) for the author(s) of this article can be found under https://doi.org/10.1002/adfm.202509532

© 2025 The Author(s). Advanced Functional Materials published by Wiley-VCH GmbH. This is an open access article under the terms of the Creative Commons Attribution License, which permits use, distribution and reproduction in any medium, provided the original work is properly cited.

DOI: 10.1002/adfm.202509532

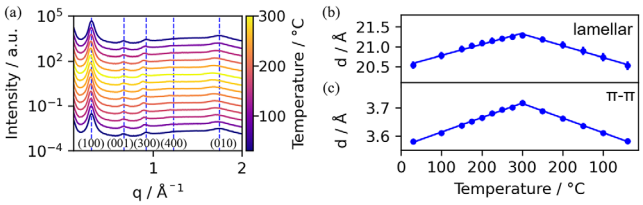

Figure 1. WAXS of isotropic, free-standing PM6. a) Line cuts of the 2D WAXS data. The change in peak position with temperature is indicated by the dashed lines. The curves are shifted in intensity for clarity. b) and c) show corresponding calculated *d*-spacing for the (100) lamellar stacking (b) and the (010) π–π stacking (c). The solid lines indicate the fit to obtain the thermal expansion coefficient.

thermal expansion behavior: 1) initial nanostructure within the film, 2) the distinctly different expansion coefficients between the substrate and thin film as well as 3) rearrangements on the nanoscale during heating. To decipher the influence of these individual factors, we systematically investigate the temperature behavior of the isotropic material with an increasing number of constraints, to finally explain the behavior in thin films relevant for future devices that regularly heat up during operation.

2. Results

2.1. Thermal Expansion Behavior of Isotropic, Free-Standing PM6

To understand the thermal expansion behavior of PM6 in thin films, we initially examine the bulk behavior of PM6 as a function of temperature in a sample that is spatially isotropic and free-standing (i.e., without a substrate). Therefore, a PM6 flake as-synthesized and received from the commercial supplier was chosen. To ensure that the observed changes solely result from the thermal response of the PM6 and not from rearrangements within the material during heating, an initial thermal treatment up to 300 °C in vacuum was applied to structurally relax the sample. The structurally relaxed sample was then heated from 30 to 300 °C and cooled back down to 40 °C during WAXS measurements (see Figure S1, Supporting Information). In the 2D WAXS pattern and the corresponding extracted line cuts, five peaks can be observed as indicated by the blue lines in **Figure 1a**. The peaks at 0.31, 0.92 and 1.23 $Å^{-1}$ are assigned to the (100), (300), and (400) lamellar stacking, the peak at 0.67 $Å^{-1}$ is assigned to the (001) backbone stacking and the peak at 1.75$Å^{-1}$ is assigned to the (010) π–π stacking. The lamellar and π–π peaks shift to smaller *q*-values during heating and higher *q*-values during cooling, while no shift with temperature is observed in the backbone direction. The *q*-values are linked with the *d*-spacing of the respective scattering planes by $d = \frac{2\pi}{q}$, therefore the shift is associated with thermal expansion and contraction of the respective spacing during heating and cooling (see Figure 1b,c). We fitted the d-spacing with a linear function $d(T) = d_0(1 + \alpha T)$, to extract α, the coefficient of the thermal expansion (CTE). $d(T)$ describes the linear growth of the lattice spacing, where d_0 is the lattice spacing at temperature T_0, which is set at 0 °C for this analysis.[15–17] As shown in Figure 1b,c, the lamellar stacking as well as the π–π-stacking show a symmetric expansion for heating and cooling, with CTE values shown in **Table 1**. Although a linear fit describes the experimental data well, recent studies have shown that the expansion might not be described by a single linear behavior.[18] Therefore we tested splitting the data into two temperature regimes and fitting them separately. This alternative analysis is provided in the Supporting Information Section S1. For the π–π stacking, the improvement in fit quality is marginal, and the single linear CTE remains a good description. For the lamellar stacking, a slightly improved fit is obtained when splitting at ≈200 °C. However, the change in R^2 is small, and thus the linear fit remains an appropriate model.

2.2. Thermal Expansion Behavior of Anisotropic, Free-Standing PM6

Films deposited from solution are no longer isotropic but are known to exhibit anisotropic distributions of ordered fractions and, hence have an initial anisotropic nanoscale arrangement.[9] To investigate the consequence of these anisotropic nanostructures on the thermal expansion behavior, PM6 was dissolved in chloroform and drop-cast to obtain a thick film. The resulting film was scraped off the glass, coiled up, and then inserted into a capillary to be measured in free-standing geometry to solely examine the influence of this nanostructure. This sample was further structurally relaxed by an initial heating to 300 °C in a vacuum. Subsequently, the same temperature protocol as for the isotropic sample was repeated during WAXS measurements. The resulting 2D WAXS patterns exhibit an anisotropy of the scattering rings (see Figure S4, Supporting Information). The anisotropic WAXS measurements are examined along two perpendicular axes ***a*** and ***b*** through the relevant intensity maxima, as shown in Figure S5 (Supporting Information). The corresponding line cuts with the (100), (001), (300), and (010) peaks, are shown in **Figure 2**. In ***a***-direction, the four peaks are located at room temperature at 0.31, 0.67, 0.93 $Å^{-1}$, 1.74 $Å^{-1}$, and in

Table 1. Coefficient of thermal expansion of free-standing PM6 for isotropic and anisotropic samples. The values for the anisotropic sample are given in *a*- and *b*-axis direction (see Figure S5, Supporting Information).

Isotropic, free-standing PM6			Anisotropic, free-standing PM6		
Crystal plane	Thermal expansion coefficient α (30–300 °C) × 10^{-4} K^{-1}	Thermal expansion coefficient α (300–40 °C) × 10^{-4} K^{-1}	Crystal plane	Thermal expansion coefficient α (30–300 °C) × 10^{-4} K^{-1}	Thermal expansion coefficient α (300–40 °C) × 10^{-4} K^{-1}
(100)	1.36 ± 0.07	1.33 ± 0.05	$(100)_a$	2.01 ± 0.10	1.79 ± 0.11
			$(100)_b$	1.49 ± 0.06	1.36 ± 0.06
(010)	1.45 ± 0.03	1.35 ± 0.02	$(010)_a$	1.68 ± 0.06	1.56 ± 0.04
			$(010)_b$	1.61 ± 0.05	1.47 ± 0.06

© 2025 The Author(s). Advanced Functional Materials published by Wiley-VCH GmbH

16163028, 2025, 48, Downloaded from https://advanced.onlinelibrary.wiley.com/doi/10.1002/adfm.202509532 by Universitaet Bayreuth, Wiley Online Library on [24/03/2026]. See the Terms and Conditions (https://onlinelibrary.wiley.com/terms-and-conditions) on Wiley Online Library for rules of use; OA articles are governed by the applicable Creative Commons License

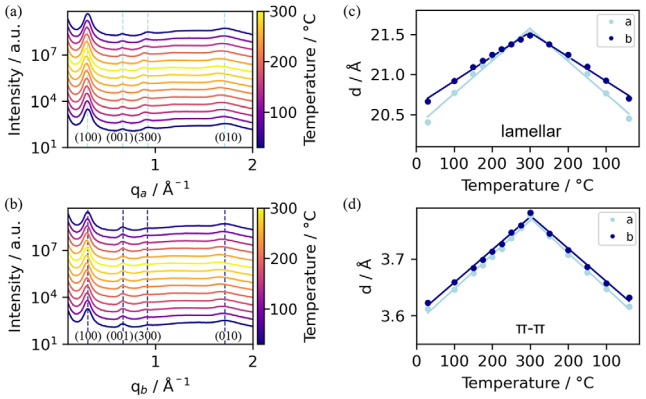

Figure 2. WAXS of anisotropic, free-standing PM6. a,b) 1D line cuts of the 2D WAXS data divided in the directions of the anisotropy along a- and b-direction. The change in peak position with temperature is indicated by the dashed lines. The curves are shifted in intensity for clarity. c,d) show corresponding calculated *d*-spacing for the (100) lamellar stacking (c) and the (010) π–π stacking (d). The solid lines indicate the fit to obtain the thermal expansion coefficient. The errors in the *d*-spacing values are below $\pm 2 \times 10^{-3}$ Å.

b-direction at 0.30, 0.67, 0.92, 1.73 Å^{-1}, with fit errors below $\pm 2 \times 10^{-3}$ Å^{-1}, showing an anisotropy in the stacking distances in the WAXS pattern of the free-standing, curled up sample. It is worth noting that the anisotropic sample exhibits three lamellar reflections, whereas the isotropic sample shows four, suggesting less long-range order in the anisotropic sample. The lamellar and the π–π stacking distances symmetrically expand and contract during heating and cooling in both, ***a***- and ***b***-direction, each returning to their initial value. Although there is an offset in the *d*-spacing values for the ***a***- and ***b***-direction at low temperatures, both directions reach a similar value at 300 °C for lamellar and π–π stacking. The initial offset changes the slope and hence the CTE value (see Table 1). Notably, the CTE in ***a***- and ***b***-direction differ by a factor of ≈1.35 for lamellar expansion and ≈1.04 for π–π stacking expansion due to the pre-structured nature of the sample.

2.3. Film Formation of PM6

To clarify the origin of the initial anisotropic nanoscale arrangements in solvent-deposited samples, time-resolved GIWAXS measurements were conducted during the blade-coating of PM6 thin films. Compared to other techniques like spin-coating, the film formation process is typically slower during blade-coating,[19] allowing for a more detailed analysis of the structural evolution. After solution deposition, a broad peak at ≈1.4 Å^{-1} appears (see Figure S6, Supporting Information), corresponding to the scattering of the solution. As the solvent evaporates, the solution peak gradually disappears, while the characteristic peaks associated with the lamellar (100), backbone (001), and π–π (010) stacking emerge. This corresponds to the development of long-range order in the PM6 film during solvent evaporation. The lamellar and π–π stacking peaks are observed along both q_z and q_r, indicating two predominant orientations within the film, corresponding to edge-on and face-on fractions. The vertical *(h00)* and horizontal *(0k0)* peaks are associated with edge-on crystallites, while the horizontal *(h00)* and vertical *(0k0)* peaks result from face-on crystallites. The (001) backbone peak, observed in horizontal direction, results from both, face-on and edge-on crystallites.

To analyze the evolution of these two crystallite fractions in detail, cake cuts were performed along q_z and q_r, and the (100) lamellar and solution peaks were fitted. **Figure** 3a displays the temporal evolution of the intensity of the solution peak (gray) and the intensity of the lamellar peaks (black = face-on, red = edge-on). Shortly after solution deposition, the solution peak intensity decreases, while the intensity of the lamellar peaks increases. After 5.6 s, the solution peak is no longer detectable, while the intensity of the lamellar peaks levels off, indicating that the film formation process is finalizing once the solvent is fully evaporated. This is furthermore supported by the evolution of the lamellar *d*-spacing values, shown in Figure 3b. After solvent removal, indicated by the gray line, the *d*-spacing stabilizes. The edge-on oriented and face-on oriented crystallites exhibit distinct formation mechanisms: While the edge-on stacking contracts during solvent evaporation, which is the typically observed behavior,[20,21] the face-on stacking expands and behaves differently with the slope as a function of time for the face-on fraction being steeper than for the edge-on fraction. The evolution of the coherence lengths of both stacking directions, shown in Figure 3c, exhibits qualitatively comparable behavior but has a different final value. During the evaporation of the solvent, the coherence length increases until it becomes relatively stable upon full evaporation of the solvent. The kinetics of formation of edge-on and face-on fractions hence differ and the differences in initial anisotropic nanoscale arrangements arise during solution deposition.

2.4. Thermal Expansion Behavior of PM6 on a Solid Substrate

To examine PM6 thin film on a solid substrate with initial anisotropic nanoscale arrangements and the effect of local rearrangements during heating, PM6 films were spin-cast onto Si wafers, dried, and subsequently analyzed with in situ GIWAXS using the same temperature protocol as before. The resulting GIWAXS cake cuts are shown in **Figure** 4a,b. For the as-cast film, three different peaks at 0.32, 0.95, and 1.70 Å^{-1} are identified in the vertical direction (along q_z), corresponding to the first and third order of lamellar stacking (100), (300) of the edge-on crystallites and the π–π stacking (010) of the face-on crystallites. In the horizontal direction (along q_r), peaks at 0.29, 0.60 and

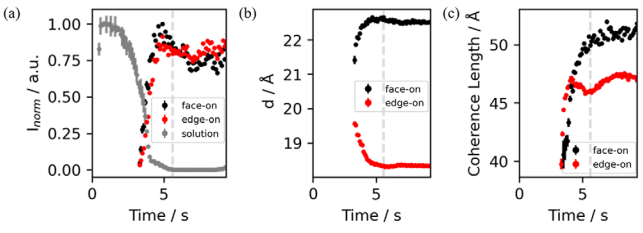

Figure 3. Time-resolved GIWAXS of PM6 film formation. a) Normalized intensity of solution peak in comparison with lamellar edge-on and face-on peak. Calculated b) *d*-spacing values and c) coherence lengths for the two lamellar stacking directions. The gray line indicates the time of complete solvent evaporation.

© 2025 The Author(s). Advanced Functional Materials published by Wiley-VCH GmbH

16163028, 2025, 48, Downloaded from https://advanced.onlinelibrary.wiley.com/doi/10.1002/adfm.202509532 by Universitaet Bayreuth, Wiley Online Library on [24/03/2026]. See the Terms and Conditions (https://onlinelibrary.wiley.com/terms-and-conditions) on Wiley Online Library for rules of use; OA articles are governed by the applicable Creative Commons License

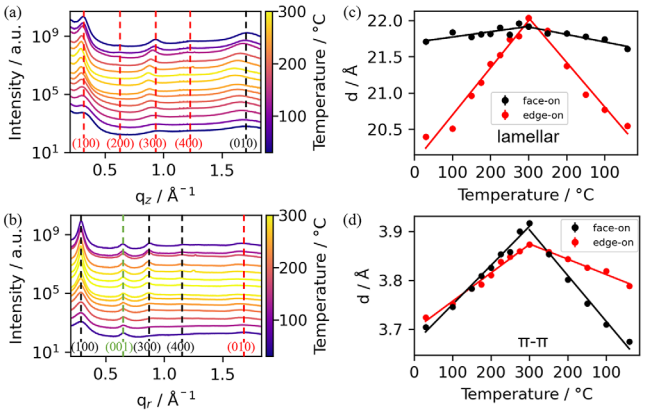

Figure 4. GIWAXS of PM6 on a solid substrate. 1D line cuts for the a) out-of-plane and b) in-plane directions showing the shift of the (h00), (00l), and (0k0) peaks in out-of-plane direction as indicated by the lines. The face-on peaks are indicated by black and the edge-on peaks by red. In contrast, no shift of the (h00) peaks is detected in the in-plane direction. The (001) peak resulting from the edge-on and face-on crystallite is indicated by green. The curves are shifted in intensity for clarity. c,d) show corresponding calculated *d*-spacing for the (100) lamellar stacking (c) and the (010) π–π stacking (d). The solid lines indicate the fit to obtain the thermal expansion coefficient.

1.69 Å^{-1} are detected. These peaks correspond to the face-on lamellar (100), backbone (001), and edge-on π–π (010) stacking reflections, respectively. We note that the absence of higher orders of lamellar stacking is a sign of less ordered crystallites prior to heating.[13] Note that the (100) *d*-spacing of the face-on crystallites (≈21.6 Å) is distinctly larger than that of the edge-on crystallites (≈19.9 Å)

The increase and addition of new peaks (see Figure S7 and Table S2, Supporting Information) observed in the GIWAXS measurements during heating and cooling reveal that ordering takes place in the spin-coated film on the silicon substrate, as expected. Thus, after the completed experiment, the lamellar stacking *(h00)* with $h = 1, 2, 3, 4$ occurs in the vertical direction for the edge-on crystallites and with $h = 1, 3, 4$ in the horizontal direction for the face-on crystallites. Furthermore, orientational preference is increased during the temperature cycle.

Overall, several expansion and contraction signatures are now present when the film is experiencing the temperature protocol while on a substrate and the origin of these needs to be deciphered.

A systematic peak shift of the edge-on lamellar peak and the edge-on and face-on π–π peaks can be detected (deviation from the vertical dashed lines) in Figure 4a,b during heating and cooling. In contrast, minimal changes in *q*-positions are detected for the face-on lamellar stacking parallel to the substrate. At the highest temperature, the lamellar stacking for both, the face-on and edge-on contributions, reach a similar maximum stacking distance (see Figure 4c,d). The initial lamellar *d*-spacing differs for edge-on versus face-on and returns to a comparable value upon cooling, respectively. The described behavior so far is analogous to that of the anisotropic, free-standing film. However, for the π–π stacking, the *d*-spacing of the edge-on fraction remains smaller than that of the face-on fraction at the maximum temperature.

Furthermore, while a symmetric behavior is observed for the face-on fraction, a reduced contraction arises during the cooling for the π–π stacking of the edge-on fraction. Here, the final *d*-spacing value differs by a factor of 1.02 compared to the initial value, reducing the CTE value during cooling (see **Table 2**). We point out that the *d*-spacing is corrected for refraction effects, as described in Section S2 and Figure S8 (Supporting Information).

For the edge-on lamellar stacking and both π–π stackings, the CTE values are within the range of the values for the free-standing samples and reported for P3HT, PBTTT, and P(NDI2OD-T2),[16,17,22] while the CTE for the face-on lamellar stacking is significantly lower. To examine the origin for the reduction in CTE for the edge-on π–π stacking and the face-on lamellar stacking, the measurement is repeated at several different incident x-ray angles below (0.76°, 0.081°) and above (0.096°, 0.106°) the critical angle (0.091°), as shown in Figure S9 (Supporting Information). For the edge-on π–π stacking, a constant initial *d*-spacing is observed for both surface-sensitive (below critical angle) and bulk-sensitive measurements (above critical angle). However, the maximum *d*-spacing at 300 °C is larger at the surface than in the bulk and consequently makes the observed CTE decrease within the bulk of the sample. For the face-on lamellar stacking, the CTE behavior at surface versus bulk is similar, but the overall situation is significantly different. Here, already the initial *d*-spacing is lower on the surface of the sample than in the bulk and also the maximum *d*-spacing at 300 °C follows this behavior. Consequently, this also results in an increased CTE below the critical angle, and a reduced CTE for bulk measurements, but due to the initial stacking configuration.

For OSC devices that heat up and cool during standard usage, the behavior of PM6 with temperature is particularly relevant in blends with acceptor materials. To investigate the thermal expansion behavior of PM6 in a blend, we performed the same heating protocol on a PM6:Y6 thin film. In this case, we analyze the thermal expansion behavior of the (300) lamellar stacking peak instead of the (100) peak, since diffraction peaks from Y6 overlap with the (100) peak of PM6. Figure S10 (Supporting Information) shows the comparison of the neat and blend data from the (300) lamellar stacking peak for both samples. In the PM6:Y6 blend, no edge-on fraction is observed, while the face-on lamellar stacking exhibits similar *d*-spacing values and CTEs as in the neat PM6.

2.5. Thermal Influence on Coherence Length

For polymeric materials, the peak width cannot directly be linked with the crystallite size, since the peak width also has contributions due to the para-crystalline nature of the material. This typically leads to an underestimation of the actual crystallite size.[23] Multiple higher orders are not observed for all stacking directions and measurement conditions, therefore other analysis methods to determine the crystallite size, such as the Williamson–Hall and Warren–Averbach methods, are not suitable.[13] We therefore use the Debye–Scherrer equation to estimate *FWHM* is the full width at half maximum of the peak. The extracted values of the coherence length of the (100) signal are shown in **Figure** 5a as a function of temperature. The coherence length

© 2025 The Author(s). Advanced Functional Materials published by Wiley-VCH GmbH

16163028, 2025, 48, Downloaded from https://advanced.onlinelibrary.wiley.com/doi/10.1002/adfm.202509532 by Universitaet Bayreuth, Wiley Online Library on [24/03/2026]. See the Terms and Conditions (https://onlinelibrary.wiley.com/terms-and-conditions) on Wiley Online Library for rules of use; OA articles are governed by the applicable Creative Commons License

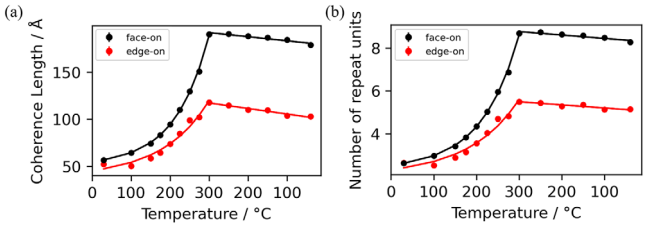

Figure 5. Calculated a) coherence length L, and b) number of repeat units n of the lamellar (100) peak for PM6 on a solid substrate. The solid lines indicate the fit to obtain the crystallite growth coefficient.

increases during heating and slightly decreases during cooling for both crystallite fractions within the film. In more detail, both lamellar stackings start at roughly the same value ≈50 Å, however the coherence length of the face-on stacking grows up to 190 Å while the coherence length in the edge-on direction grows only to 118 Å. Interestingly, the growth of the coherence length $L(T)$ during the heating process shows an exponential character, that can be fitted with $L(T) = L_0 (1 + \beta)^T + c$, where $L(T)$ and L_0 is the coherence length at T and T_0 ($T_0 = 0$ °C) respectively, β is the growth rate and c is a constant offset (see Table 2). Since the coherence length increases with an exponential characteristic, the values cannot be compared with literature values where a linear increase of the coherence length has been reported instead.[16,17]

As the growth of the coherence length $L(T)$ is a combination of the thermal expansion of the polymer and the increase of the correlation length of repeating units, the number of repeat units is analyzed as well. We estimate it as the ratio of the coherence length $L(T)$ and the lattice spacing $d(T)$, i.e., $n = \frac{L(T)}{d(T)}$. Similar to the coherence length, $n(T)$ exhibits exponential growth during the heating procedure and remains relatively stable during the cooling process for both lamellar directions, as shown in Figure 5b. Initially, $n(T)$ has similar values for both lamellar directions, however, after the thermal treatment, there are 1.37 times the number of repeat units in face-on lamellar stacking compared to the edge-on lamellar stacking. This ratio is similar to the coherence length, showing that the growth behavior of the crystallites is dominated by the increase in coherence length in comparison to the thermal expansion of the d-spacing.

Due to the low intensity and amorphous background of the π–π stacking peaks, the width of the π–π stacking is not quantitatively analyzed.

2.6. Orientation Behavior

The thermal response of the crystallite orientation within the bulk of the film is analyzed by examining the intensity of the (100) peak as a function of the polar angle. The intensity is corrected regarding the polar angle with $I_{corrected} = I_{measured} \times sin(\chi)$ to compensate for the sample symmetry and to obtain signal intensities comparable to the amount of material for a particular orientation. The contributions were initially constant, but are now corrected using a sine-shaped, isotropic background, along with edge-on and face-on fractions. In the corrected data crystallites that scatter to polar angles below 45° are defined as edge-on, while those that scatter to above 45° are defined as face-on, as shown in Figure S11 (Supporting Information). The resulting bar chart shown in **Figure 6**a shows that the thin film exhibits a more isotropic characteristic before the heating procedure with a slight preference for edge-on orientation. During the heating procedure, the ratio of face-on-oriented fractions increases while the edge-on and isotropic contributions decrease. The orientation remains unchanged during cooling.

It was previously reported that differences in the growth mechanism during the sample deposition can result in different orientations for the surface and the bulk of a sample.[24,25] Therefore, GIWAXS is measured with an angle below (β_b) the critical angle (β_c) to probe the surface layers of the film. The same analysis as

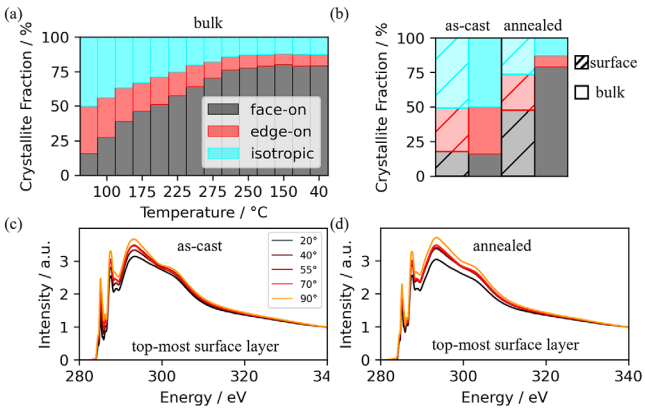

Figure 6. GIWAXS of PM6 on a solid substrate. a) Evaluated bulk orientation of the thin film. b) Comparison of orientation of surface layers (hatched) and bulk orientation (filled) of as-cast (left) and annealed (right) sample. c,d) NEXAFS spectra of the as-cast (c) and annealed (d) sample at five different angles.

Table 2. Thermal expansion values in PM6 in the horizontal and vertical direction for the (100) lamellar, (010) π–π, and (001) backbone stacking direction. The thermal expansion coefficient is defined by the change of the d-spacing with temperature and the growth rate is defined by the growth of the coherence length during heating.

	Crystal plane	Direction	Thermal expansion coefficient α (30–300 °C) × 10^{-4} K^{-1}	Thermal expansion coefficient α (300–40 °C) × 10^{-4} K^{-1}	Growth rate β (30–300 °C) × 10^{-3} K^{-1}
face-on	(100)	↔	0.34 ± 0.09	0.47 ± 0.07	11.6 ± 0.5
	(010)	↕	2.18 ± 0.10	2.21 ± 0.12	N/A
edge-on	(100)	↕	3.27 ± 0.20	2.43 ± 0.13	8.3 ± 1.9
	(010)	↔	1.57 ± 0.07	0.79 ± 0.05	N/A
both	(001)	↔	0.29 ± 0.07	0.15 ± 0.05	N/A

© 2025 The Author(s). Advanced Functional Materials published by Wiley-VCH GmbH

16163028, 2025, 48, Downloaded from https://advanced.onlinelibrary.wiley.com/doi/10.1002/adfm.202509532 by Universitaet Bayreuth, Wiley Online Library on [24/03/2026]. See the Terms and Conditions (https://onlinelibrary.wiley.com/terms-and-conditions) on Wiley Online Library for rules of use; OA articles are governed by the applicable Creative Commons License

carried out for β_b results in Figure 6b and Figure S12 (Supporting Information). Before the heating procedure, the distribution of orientations is comparable in the bulk (β_c) and surface layers (β_b). In contrast, after the thermal treatment, the face-on orientation within the surface layers is reduced in comparison to the bulk. An increased edge-on oriented fraction is identified. As GIWAXS at an incident angle below the critical angle still probes ≈10 nm into the sample,[26] the orientation of the top-most surface layer (≤ 3 nm)[27,28] was analyzed using near-edge X-ray absorption fine structure (NEXAFS) spectroscopy, as shown in Figure 6c,d. The analysis shows that before heating, an overall preference for edge-on orientation is found at the surface, with an average tilt angle of the conjugated backbone of $\langle\alpha\rangle = 58 \pm 1°$. The heating procedure increases the edge-on orientation of the surface since the average tilt of the backbone increases to $\langle\alpha\rangle = 64 \pm 1°$. These results are in line with the GIWAXS data collected in the surface-sensitive measurements. Furthermore, the reported values for the backbone tilt are similar to previously reported values for PM6.[9]

3. Discussion

The most striking observation from this study is the distinct thermal expansion behavior of face-on and edge-on fractions in PM6 thin films, with the face-on fraction exhibiting a much smaller expansion coefficient of the (100) peak (0.34×10^{-4} K^{-1}) compared to the edge-on fraction (3.27×10^{-4} K^{-1}). These different para-crystalline populations (i.e., face-on and edge-on) also exhibit other distinct characteristics, namely their kinetic formation and consequently different initial (100) *d*-spacings (≈21.7 Å for face-on and ≈19.6 Å for edge-on). In particular, from the in situ coating experiments, the face-on fraction exhibits an increase in *d*-spacing during film drying while the edge-on fraction exhibits a decrease in *d*-spacing as the film dries (Figure 3b). These observations suggest that face-on and edge-on fractions in PM6 films have different formation mechanisms and possess different molecular packing, though the precise details of these packing differences remain unclear. Compared to the free-standing samples, the edge-on fraction in the film has similar (100) *d*-spacing and CTE, suggesting the face-on fraction might represent a "thin-film phase" of PM6. Additional differences in the observed thermal behavior of face-on and edge-on fraction included the reduced expansion and symmetry breaking during cooling that occurs for the π–π stacking in substrate direction, i.e., for the edge-on π–π stacking, in the bulk of the film. The depth-dependence of this behavior, with higher thermal expansion at the surface, suggests a secondary influence of the substrate, with silicon exhibiting a 100-fold lower CTE compared to PM6. Note that the effect of the substrate is not likely to explain the low CTE of the (100) of face-on fraction as this fraction already has a large *d*-spacing when formed from solution and the changes in CTE cannot be explained by a depth dependence of the initial and maximum *d*-spacing value. To establish relevance to solar cell devices that employ a blend of PM6 with an NFA, a film of PM6 blended with Y6 was also studied. While in the PM6:Y6 blend only face-on crystallites were observed, they exhibited the same behavior, namely a larger initial *d*-spacing (compared to edge-on crystallites in neat PM6) and low thermal expansion co-efficient. Consequently, the characteristics of the face-on crystallites observed in neat films are not altered by the presence of Y6.

4. Conclusion

Through the application of in situ WAXS and GIWAXS, we have characterized the thermal expansion behavior of PM6 in a stepwise manner, by incrementally increasing the sample complexity. The intrinsic expansion behavior could be revealed by analyzing a free-standing isotropic sample, resulting in a symmetric increase and decrease of the *d*-spacing for both the lamellar and π–π stacking. In thin films, however, altered thermal expansion behavior is observed, with the (100) CTE reduced by an order of magnitude between face-on and edge-on fractions. This difference is attributed to different packings of face-on and edge-on fractions that form during coating, supported by in situ GIWAXS measurements of film formation. In addition, an asymmetric expansion and contraction for the edge-on π–π stacking is observed. By comparing the expansion in the bulk and at the surface of the sample, the edge-on π–π stacking behavior is attributed to a mismatch between the thermal expansion of the substrate and the sample, resulting in a decreased thermal expansion in the bulk. These findings emphasize the complex relationship between substrate interaction, material pre-structuring, and thermal behavior, which must be considered for future devices.

5. Experimental Section

Material and Sample Preparation: All measurements were done on PBDB-T-2F (PM6) with a molecular weight of 108 kDa and a dispersity of 2.9, which was purchased from Ossila. For the isotropic, free-standing sample, the material was used as received and measured in a capillary. For the anisotropic, free-standing sample, PM6 was dissolved in chloroform and drop-cast on a watch glass. The resulting thick film was scraped off, coiled, and measured in a capillary. For the in situ blade-coating, PM6 was dissolved in chloroform (7.3 mg mL^{-1}) and blade-coated with a velocity of 10 mm s^{-1}. The PM6 thin films, used for temperature-resolved GIWAXS, were spin-cast from a chloroform solution (4 mg mL^{-1}) on bare silicon substrates with a coating speed of 3000 rpm for 60 s. Before spin-coating, the Si substrates were cleaned in an ultrasonic bath using soap water (Hellmanex), water, acetone, isopropanol, followed by an oxygen plasma treated for 10 min.

Methods—WAXS: The WAXS measurements were performed on a laboratory system at the University of Bayreuth (Xeuss 3.0, Xenocs SAS, Grenoble, France) with a Cu Kα source (λ = 1.54 Å) with a HFSX350 temperature stage (Linkam, UK). The scattering patterns were recorded with a Dectris EIGER 2R 1 M detector, with 1028 × 1062 pixels and a pixel size of 75 µm × 75 µm, and a sample-to-detector distance of 52 mm. The beam size was adjusted to 0.5 mm × 0.5 mm. A heating rate of 10 °C min^{-1} and each temperature step was held for 15 min.

Methods—GIWAXS: The in situ blade-coating and heating GIWAXS measurements were performed with an energy of 15 keV (λ = 0.827 Å) at the SAXS/WAXS beamline at the Australian Synchrotron.[29] A Dectris Pilatus3-2 M (in-vacuum) detector with a pixel size of 0.172 mm × 0.172 mm was used.

For the time-resolved blade-coating measurements a sample-detector distance of 689 mm was used and the measurements were performed in air using a custom-made setup. The obtained in situ *d*-spacing values are uncorrected.

The temperature-resolved measurements were performed with a sample-detector distance of 704 mm. The measurements were performed in a vacuum using a Linkam HFSX350 temperature stage. The temperature was increased and decreased at a rate of 5 °C min^{-1} to the desired temperature during the heating and cooling process. At each temperature step, the temperature was held for 5 min to reach the equilibrium temperature before alignment and measurement. The alignment was redone at

© 2025 The Author(s). Advanced Functional Materials published by Wiley-VCH GmbH

16163028, 2025, 48, Downloaded from https://advanced.onlinelibrary.wiley.com/doi/10.1002/adfm.202509532 by Universitaet Bayreuth, Wiley Online Library on [24/03/2026]. See the Terms and Conditions (https://onlinelibrary.wiley.com/terms-and-conditions) on Wiley Online Library for rules of use; OA articles are governed by the applicable Creative Commons License

every temperature to eliminate the effects of the thermal expansion of the stage and the substrate. The sample was moved to a new position for each measurement to minimize beam damage.

The GIWAXS data were processed using NIKA[30] in Igor Pro and by Python scripts.

Methods—NEXAFS Spectroscopy: The NEXAFS measurements were performed ex situ at the soft X-ray spectroscopy beamline at the Australian Synchrotron.[31] The "annealed" sample underwent all the temperature steps used for the GIWAXS measurements, with each temperature being held for 10 min before the NEXAFS measurements were performed. The K-edge of the PM6 was measured at different angles to identify the average tilt angle of all polymer backbones within the examined sample volume. The measured spectra are fitted, and by the intensity of the π^*-orbital, the average tilt angle of the π-conjugated backbone was calculated.[28] The data were analyzed using the QANT software.[32]

Supporting Information

Supporting Information is available from the Wiley Online Library or from the author.

Acknowledgements

M.K. and E.M.H. acknowledge financial support from Deutsche Forschungsgemeinschaft (INST91/443-1), the DFG International Research Training group (IRTG 2818) Optical excitations in organic and inorganic semiconductors (OPTEXC) and from the German Academic Exchange Service (DAAD). This work was supported by the Australian Research Council (DP230100170). This research was undertaken on the SAXS/WAXS and Soft X-Ray beamlines at the Australian Synchrotron, part of ANSTO.

Conflict of Interest

The authors declare no conflict of interest.

Data Availabilty Statement

The data that support the findings of this study are available from the corresponding author upon reasonable request.

Keywords

aggregate species, asymmetric thermal expansion, thermal properties

Received: April 15, 2025
Revised: May 23, 2025
Published online: June 18, 2025

[1] B. C. Thompson, J. M. J. Fréchet, *Angew. Chem.* **2008**, *47*, 58.
[2] H. Sirringhaus, *Adv. Mater.* **2014**, *26*, 1319.
[3] J. Rivnay, S. Inal, A. Salleo, R. M. Owens, M. Berggren, G. G. Malliaras, *Nat. Rev. Mater.* **2018**, *3*, 1.
[4] B. Russ, A. Glaudell, J. J. Urban, M. L. Chabinyc, R. A. Segalman, *Nat. Rev. Mater.* **2016**, *1*, 16050.
[5] N. R. E. Laboratory, Best Research-Cell Efficiency Chart, www.nrel.gov/pv/assets/pdfs/best-research-cell-efficiencies.20200104.pdf (accessed: January 2025).
[6] L. Zhu, M. Zhang, J. Xu, C. Li, J. Yan, G. Zhou, W. Zhong, T. Hao, J. Song, X. Xue, Z. Zhou, R. Zeng, H. Zhu, C. C. Chen, R. C. I. MacKenzie, Y. Zou, J. Nelson, Y. Zhang, Y. Sun, F. Liu, *Nat. Mater.* **2022**, *21*, 656.
[7] Y. Cui, Y. Xu, H. Yao, P. Bi, L. Hong, J. Zhang, Y. Zu, T. Zhang, J. Qin, J. Ren, Z. Chen, C. He, X. Hao, Z. Wei, J. Hou, *Adv. Mater.* **2021**, *33*, 2102420.
[8] D. Kroh, F. Eller, K. Schötz, S. Wedler, L. Perdigón-Toro, G. Freychet, Q. Wei, M. Dörr, D. Jones, Y. Zou, E. M. Herzig, D. Neher, A. Köhler, *Adv Funct. Mater.* **2022**, *32*, 2205711.
[9] D. Neusser, B. Sun, W. L. Tan, L. Thomsen, T. Schultz, L. Perdigón-Toro, N. Koch, S. Shoaee, C. R. McNeill, D. Neher, S. Ludwigs, *J. Mater. Chem. C* **2022**, *10*, 11565.
[10] N. Yao, J. Wang, Z. Chen, Q. Bian, Y. Xia, R. Zhang, J. Zhang, L. Qin, H. Zhu, Y. Zhang, F. Zhang, *J. Phys. Chem. Lett.* **2021**, *12*, 5039.
[11] R. Ma, G. Li, D. Li, T. Liu, Z. Luo, G. Zhang, M. Zhang, Z. Wang, S. Luo, T. Yang, F. Liu, H. Yan, B. Tang, *Sol. RRL* **2020**, *4*, 2000250.
[12] Q. Fan, T. Liu, W. Gao, Y. Xiao, J. Wu, W. Su, X. Guo, X. Lu, C. Yang, H. Yan, M. Zhang, Y. Li, *J. Mater. Chem. A* **2019**, *7*, 15404.
[13] Z. Peng, L. Ye, H. Ade, *Mater. Horiz.* **2022**, *9*, 577.
[14] S. Marina, E. Gutierrez-Fernandez, J. Gutierrez, M. Gobbi, N. Ramos, E. Solano, J. Rech, W. You, L. Hueso, A. Tercjak, H. Ade, J. Martin, *Mater. Horiz.* **2022**, *9*,1196.
[15] P. P. Huo, P. Cebe, M. Capel, *J. Polym. Sci. B Polym. Phys.* **1992**, *30*, 1459.
[16] X. Jiao, M. Statz, L. Lai, S. Schott, C. Jellett, I. McCulloch, H. Sirringhaus, C. R. McNeill, *J. Phys. Chem. B* **2020**, *124*, 10529.
[17] L. Tang, C. R. McNeill, *Macromolecules* **2022**, *55*, 7273.
[18] H. Zhao, N. Prine, S. Kundu, G. Ma, X. Gu, *JACS Au* **2024**, *4*, 4334.
[19] K. Xiong, L. Hou, M. Wu, Y. Huo, W. Mo, Y. Yuan, S. Sun, W. Xu, E. Wang, *Sol. Energy Mater. Sol. Cells* **2015**, *132*, 252.
[20] K. S. Wienhold, C. L. Weindl, S. Yin, T. Tian, M. Schwartzkopf, A. Rothkirch, S. V. Roth, P. Müller-Buschbaum, *ACS Appl. Mater. Interfaces* **2020**, *12*, 40381.
[21] S. Pröller, F. Liu, C. Zhu, C. Wang, T. P. Russell, A. Hexemer, P. Müller-Buschbaum, E. M. Herzig, *Adv. Energy Mater.* **2016**, *6*, 1501580.
[22] S. Joshi, P. Pingel, S. Grigorian, T. Panzner, U. Pietsch, D. Neher, M. Forster, U. Scherf, *Macromolecules* **2009**, *42*, 4651.
[23] D. M. Smilgies, *J. Appl. Crystallogr.* **2009**, *42*, 1030.
[24] J. Balko, G. Portale, R. H. Lohwasser, M. Thelakkat, T. Thurn-Albrecht, *J. Mater. Res.* **2017**, *32*, 1957.
[25] O. Dolynchuk, P. Schmode, M. Fischer, M. Thelakkat, T. Thurn-Albrecht, *Macromolecules* **2021**, *54*, 5429.
[26] C. J. Mueller, E. Gann, C. R. McNeill, M. Thelakkat, *J. Mater. Chem. C* **2015**, *3*, 8916.
[27] L. L. Chua, M. Dipankar, S. Sivaramakrishnan, X. Gao, D. Qi, A. T. S. Wee, P. K. H. Ho, *Langmuir* **2006**, *22*, 8587.
[28] J. Stöhr, *NEXAFS Spectroscopy*, Springer Science & Business Media, New York **2013**.
[29] N. M. Kirby, S. T. Mudie, A. M. Hawley, D. J. Cookson, H. D. T. Mertens, N. Cowieson, V. Samardzic-Boban, *J. Appl. Crystallogr.* **2013**, *46*, 1670.
[30] J. Ilavsky, *J. Appl. Crystallogr.* **2012**, *45*, 324.
[31] B. C. Cowie, A. Tadich, L. Thomsen, *AIP Conf. Proc.* **2010**, *1234*, 307.
[32] E. Gann, C. R. McNeill, A. Tadich, B. C. C. Cowie, L. Thomsen, *J. Synchrotron Radiat.* **2016**, *23*, 374.

© 2025 The Author(s). Advanced Functional Materials published by Wiley-VCH GmbH

16163028, 2025, 48, Downloaded from https://advanced.onlinelibrary.wiley.com/doi/10.1002/adfm.202509532 by Universitaet Bayreuth, Wiley Online Library on [24/03/2026]. See the Terms and Conditions (https://onlinelibrary.wiley.com/terms-and-conditions) on Wiley Online Library for rules of use; OA articles are governed by the applicable Creative Commons License